Journal of Materials Chemistry B

ROYAL SOCIETY OF CHEMISTRY

COMMUNICATION

View Article Online
View Journal | View Issue

Cite this: J. Mater. Chem. B, 2025, 13, 5769

Received 25th March 2025,
Accepted 25th April 2025

DOI: 10.1039/d5tb00689a

rsc.li/materials-b

Engineering curvature: block copolymer lithography for the fabrication of curved lipid membranes and their impact on protein–membrane interactions†

Lucia Suarez Menendez,[a] David J. Owen,[b] Nathan R. Zaccai,[b] Armando Maestro *[ac] and Alberto Alvarez-Fernandez *[a]

Studying biological membranes is essential for understanding key cellular processes such as signal transduction and ion transport, which have significant implications for developing advanced therapies for diseases like cancer and cardiovascular disorders. However, the structural complexity of these membranes presents challenges for detailed analysis, necessitating advanced techniques that are often incompatible with in-cell studies. As a result, current research has shifted toward fabricating artificial membranes that closely mimic their natural counterparts. A critical limitation remains in replicating the natural curvature of biological membranes that restricts the effectiveness of existing flat *in vitro* models. In response, this study introduces block copolymer (BCP) lithography as a method for creating nanostructured surfaces that induce controllable local membrane curvature. Lipid bilayer formation was confirmed using atomic force microscopy (AFM) and quartz crystal microbalance with dissipation monitoring (QCM-D). Subsequent investigations into clathrin assembly lymphoid myeloid-leukemia (CALM) protein interactions with curved membranes revealed a preferential binding to curved surfaces, characterized by a more homogeneous protein distribution compared to flat membranes. These findings enhance our understanding of membrane–protein interactions and cellular processes, opening up potential applications in drug delivery and biosensing.

Lipid membranes serve as fundamental platforms for the precise spatial and temporal organization of cellular components. However, their compositional complexity and nanoscale dimensions pose significant challenges for directly investigating membrane molecular mechanisms in living cells.[1] To overcome these challenges, model membrane systems that mimic the essential features of biological membranes have been developed.[2,3] Biomimetic model membranes, including liposomes and supported lipid bilayers (SLBs), are indispensable tools in bottom-up biochemistry, structural biology, and synthetic biology.[4–8] These simplified yet versatile platforms, combined with advanced characterization techniques, enable the study of molecular mechanisms underlying cellular processes (such as transport, selective permeability, and signalling) under controlled conditions that replicate physiological environments.[9,10] Moreover, by enabling the investigation of drug-membrane interactions, protein misfolding, and membrane dysfunction, model membranes are instrumental in advancing our understanding of disease mechanisms.[11–14]

Cellular membranes are dynamic, three-dimensional structures characterized by intricate curvatures, including invaginations, protrusions, and tubulations that extend across a range of length scales.[15] From the nanoscale curvature of protein–lipid complexes to the larger-scale curvature of organelles, membrane shape plays a pivotal role in processes such as vesicle trafficking, signal transduction, and cell division.[16,17] While the impact of micron-scale membrane curvature has been extensively studied, the influence of nanometer-scale curvature on protein–lipid interactions remains poorly understood. For example, the formation of clathrin-coated pits during endocytosis is linked to the generation of highly curved membrane regions.[18] This process can be facilitated by several proteins, such as the clathrin assembly lymphoid myeloid-leukaemia protein (CALM),[19] which are able to sense and respond to membrane topology.[20]

Artificial membrane systems, such as free-standing spherical liposomes, are widely employed to study membrane curvature due to their versatility in mimicking cellular shapes. While these vesicles range in size from tens of nanometers to micrometers, only the larger, micrometre-sized liposomes can be reliably manipulated into tubular or rod-like geometries to

[a] Centro de Física de Materiales (CFM) (CSIC–UPV/EHU) – Materials Physics Center (MPC), Paseo Manuel de Lardizabal 5, San Sebastián, 20018, Spain. E-mail: armando.maestro@ehu.eus, alberto.alvarez@ehu.eus
[b] Cambridge Institute for Medical Research, University of Cambridge, Cambridge CB22 7QQ, UK
[c] IKERBASQUE-Basque Foundation for Science, Plaza Euskadi 5, Bilbao, 48009, Spain

† Electronic supplementary information (ESI) available. See DOI: https://doi.org/10.1039/d5tb00689a

replicate specific membrane deformations. However, these approaches primarily address curvature on the micron scale and often lack the precision needed to control nanometric membrane morphology, which is crucial for studying curvature-sensitive processes. Furthermore, existing techniques for probing nanometric curvature, such as cryo-electron microscopy (cryo-EM), small-angle scattering, and fluorescence-based methods, have significant limitations. Cryo-EM offers static snapshots and lacks dynamic insights, scattering techniques rely on ensemble averaging, and fluorescence-based approaches may perturb membrane properties. Combined with challenges related to liposome stability and reproducibility, these constraints underscore the need for a robust, reproducible experimental system that can be used to systematically investigate protein–lipid interactions under controlled nanometric curvature conditions.

Supported lipid bilayers (SLBs) provide an attractive alternative for studying membrane processes due to their high homogeneity.[21] As a result, SLBs have been widely used to study membrane–protein interactions, as well as lipid raft formation, drug delivery mechanisms, and membrane fusion events.[22–25] SLBs are most commonly prepared through the fusion of small unilamellar vesicles, which typically range in size from 20 to 100 nm, onto planar surfaces such as polished mica or silicon substrates.[21] This approach offers significant advantages over other fabrication techniques, like Langmuir–Blodgett deposition,[26] spin-coating,[27] or rapid solvent exchange,[28] due to its scalability and versatility, as well as the ability to integrate functional molecules such as membrane proteins. In this sense, it can be inferred that since SLBs replicate the topology of the underlying substrates, using patterned or nanostructured surfaces could enable the fabrication of SLBs with greater control over membrane shape and curvature.

One of the key limitations hindering the development of this approach is the challenge of fabricating nanoscale features with precision, tunability, and scalability over large surface areas.[29] Top-down methodologies, such as electron-beam lithography and nano-imprinting, are commonly employed but require expensive equipment and time-intensive procedures.[30] In contrast, bottom-up methodologies, such as colloidal assembly and block copolymer (BCP) self-assembly, have emerged as promising alternatives, enabling the fabrication of highly tuneable and controllable nanopatterned surfaces.[31–33] In this sense, silica nanoparticle arrays fabricated *via* Langmuir–Schaefer deposition have recently been used to generate curved lipid membranes.[34] However, the potential of these surfaces for studying curvature-driven biological processes has not been explored yet. Moreover, the developed methodology offers limited tunability, highlighting the need for new fabrication approaches.

In this study, we introduce BCP lithography as a robust methodology for fabricating highly ordered nanosurfaces, enabling the creation of lipid membranes with controllable local curvature (Fig. 1). The main advantage of this fabrication approach over previous methods lies in its tunability and scalability. Key structural parameters of the final inorganic

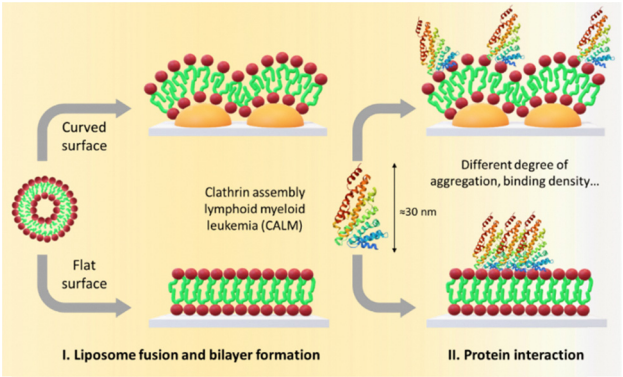

Fig. 1 Schematic showing the two main objectives of this study: first, to investigate the fabrication of lipid membranes with controllable local curvature, influenced by the nanostructured substrate created through BCP lithography; and second, to study the interaction of these curved membranes with proteins, exploring how membrane curvature impacts protein binding.

arrays, such as spatial resolution, curvature, and motif interdistance, can be precisely controlled, typically in the 20–100 nm range, by adjusting the molecular weight of the block copolymer (BCP) used as a template. Moreover, the use of spin coating enables uniform nanostructuring over large surface areas (cm^2 scale) in a straightforward and scalable manner. Using this approach, we investigated the interaction of CALM with curved 1,2-dioleoyl-*sn*-glycero-3-phosphocholine (DOPC)-based bilayers. CALM is an ideal model for studying how membrane curvature influences protein interactions and membrane dynamics. Previous studies have highlighted the critical role of the protein's N-terminal amphipathic helix (AH0), which was proposed to sense and/or induce membrane curvature, facilitating clathrin-coated vesicle formation. Therefore, this study presents a novel approach that combines advanced nanofabrication techniques with curvature-sensitive biological investigations, offering valuable insights into membrane–protein interactions at the nanoscale. By systematically exploring the effects of local curvature on membrane behaviour and protein interactions, this work addresses critical gaps in our understanding of curvature-driven processes, paving the way for future advancements in membrane biology and its biomedical applications.

Nanostructured surfaces were successfully fabricated *via* BCP lithography. To achieve this, poly(styrene)-*block*-poly(4-vinyl pyridine) (PS-*b*-P4VP) BCP was used as the starting material. A 0.5 wt% solution of the polymer in propylene glycol mono methyl ether acetate (PGMEA) was spin-coated onto silicon substrates. Atomic force microscopy (AFM) revealed a well-defined out-of-plane cylindrical structure of P4VP embedded within the PS matrix immediately after the casting process, as shown in Fig. 2A. To achieve selective functionalization, the BCP film was immersed in an aqueous solution of H_2PtCl_4, facilitating the incorporation of $PtCl_4^{2-}$ ions into the P4VP cylinders (Fig. 2B). This functionalization exploits the Brønsted base character of the P4VP block and the ionic interaction between its pyridinium moieties and platinum ions (Fig. S1, ESI†).[32] The selective nature

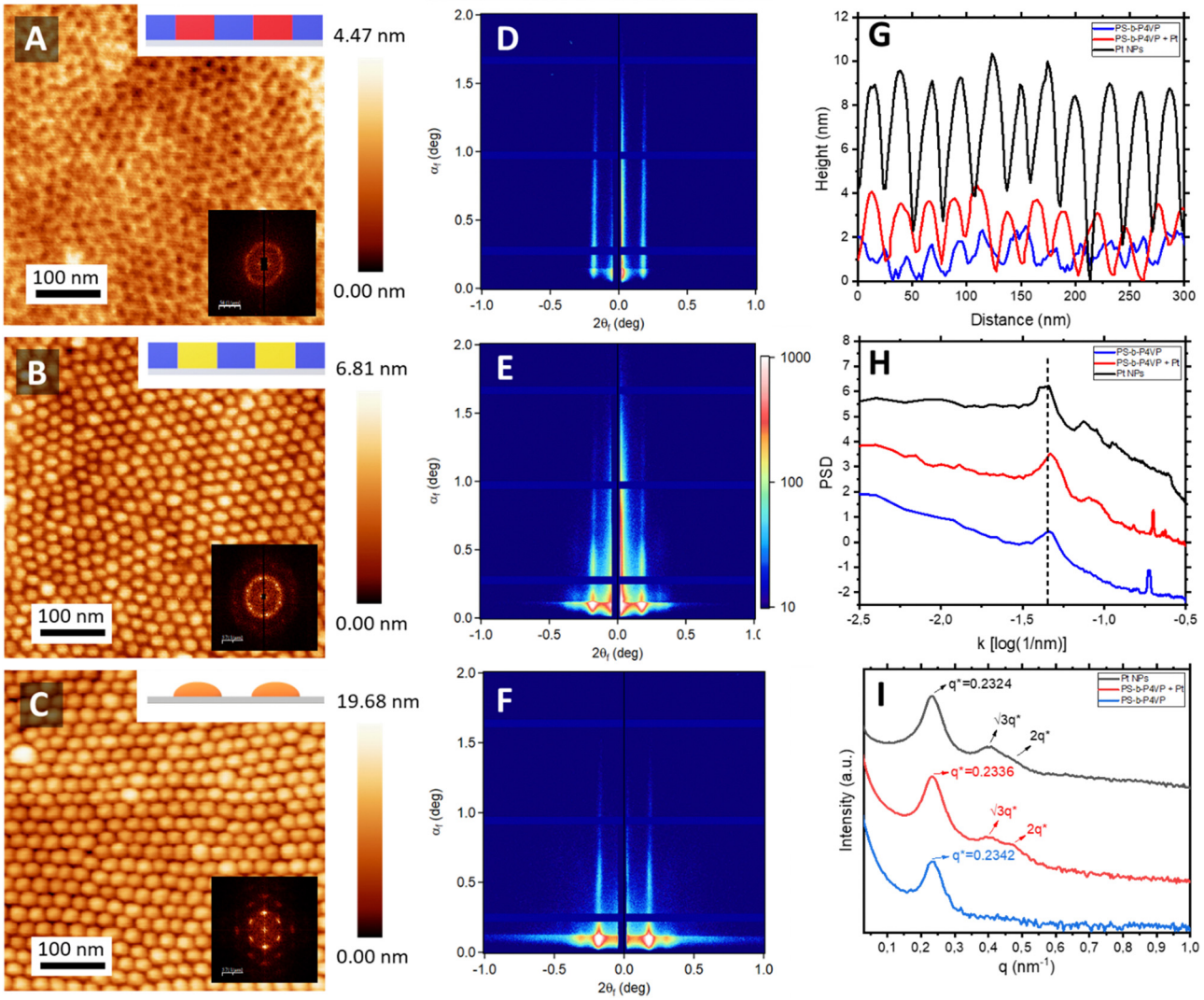

Fig. 2 AFM topographical micrographs of (A) pristine BCP film, (B) after immersion in the Pt precursor solution and (C) after the oxygen plasma treatment. (D)–(F) Corresponding 2D GISAXS profiles, (G) AFM topographical profiles, (H) PSD, and (I) 1D GISAXS line cuts.

of this interaction is corroborated by the AFM topographical profiles (Fig. 2G), while their structural stability is validated by the corresponding power spectral density (PSD) analysis (Fig. 2H).

A constant centre-to-centre distance (D_{c-c}) of 25 nm is maintained before and after selective functionalization (Fig. 2H). Following a final etching step using oxygen plasma to degrade the BCP, an array of inorganic platinum (Pt) NPs is formed. Analysis of the topographical profiles reveals an average NP height of $\approx$10 nm and a diameter of $\approx$25 nm (Fig. 2G), demonstrating the effectiveness of this methodology in producing well-defined nanostructures. GISAXS confirmed the observed morphology extended over large surface areas (mm^2). The 2D scattering patterns (Fig. 2D–F) and corresponding 1D line cuts (Fig. 2I) validate the structural order and orientation of the created features. The presence of intense Bragg rods along q_z confirms the out-of-plane orientation of the cylindrical structures, while the higher-order Bragg rods at $q/q^* = \sqrt{3}$ and 2 corroborate the observed hexagonal packing arrangement. Additionally, the D_{c-c} calculated from the q-value of the first Bragg rod aligns closely with the measurements obtained *via* AFM, confirming further the stability of the structure through the full fabrication process.

The next step in the fabrication process involved the formation of lipid bilayers onto both nanostructured and flat surfaces. In this objective, DOPC liposomes, of approximately 100 nm in diameter, were prepared by extruding a lipid suspension in tris-buffered saline (TBS) through a polycarbonate membrane with 100 nm pores. Dynamic light scattering (DLS) confirmed the homogeneity of the liposomes (Fig. S2A, ESI†). These liposomes were subsequently deposited onto the surfaces (Fig. 3A). AFM imaging verified liposome fusion and the formation of a lipid bilayer. Fig. 3B presents the topographical image of the DOPC bilayer on flat mica surfaces, while Fig. 3C displays the corresponding AFM image for the nanostructured surface. Height histograms of the Pt NP arrays, before and after lipid bilayer formation, show a height decrease of approximately 4 nm, consistent with the expected thickness

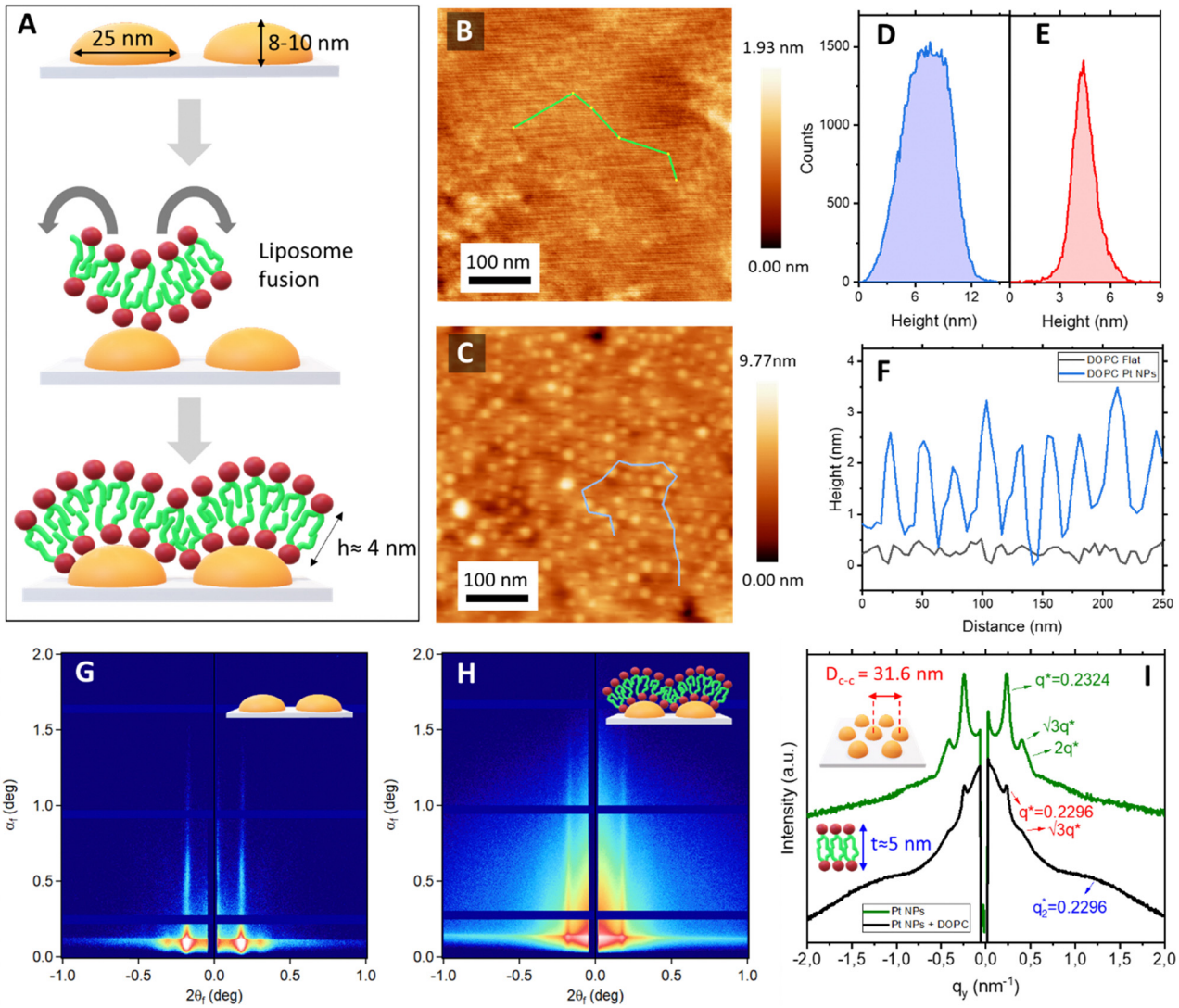

Fig. 3 (A) Schematic showing the DOPC liposome fusion and subsequent formation of the lipid bilayer. AFM topographic micrograph of a DOPC lipid bilayer on top of a (B) flat mica surface and (C) Pt NP array. AFM height histograms of (D) pristine Pt NP arrays and (E) DOPC bilayer on Pt NP array. (F) Topographical profiles showing the difference in curvature between the two different membranes. 2D GISAXS profiles of (G) Pt NPs arrays and (H) Pt NPs arrays after the deposition of the lipid bilayer. (I) Corresponding 1D GISAXS linecuts.

of a lipid bilayer (Fig. 3D and E). Local membrane curvature was confirmed from the topographical profiles (Fig. 3F). Given the D_{c-c} of 25 nm between adjacent Pt NPs, the estimated radius of curvature (R) of the features is approximately 12.5 nm. This corresponds to a mean curvature (H = 1/2R) of approximately 0.04 nm^{-1}. This nanoscale curvature induces significant alterations in lipid packing and bilayer mechanics.

GISAXS 2D scattering patterns confirmed the stability of the nanostructured surfaces during the liposome fusion and bilayer formation (Fig. 3G–I). Furthermore, the changes observed at a higher q-range after the deposition of the liposomes confirm the successful formation of the lipid bilayer onto the platinum NP array (Fig. 3H and I).

Quartz crystal microbalance with dissipation monitoring (QCM-D) is particularly well-suited for monitoring lipid bilayer deposition as it can provide real-time, label-free measurements of lipid mass accumulation and viscoelastic changes at the sensor surface during bilayer formation.[21,35] QCM-D measurements confirmed the formation of solid-supported DOPC bilayers on both planar and nanostructured surfaces (Fig. 4A and B). Both surface geometries gave similar frequency shifts ($\Delta F \approx 30$ Hz), which were consistent with typical values reported for liposome fusion and lipid bilayer formation (Fig. 4i and iii).[21] However, the dissipation was slightly larger on nanostructured surfaces (ΔD = 4 ppm) compared to planar surfaces (ΔD = 3 ppm). This increase in dissipation likely reflects the higher flexibility and dynamic behaviour of the DOPC bilayer on nanostructures. The local curvature induced by the nanostructures may result in asymmetry in lipid packing and reduced mechanical coupling with the substrate. Furthermore, the topographical heterogeneity of the nanostructures may introduce regions of varying lipid organization, further

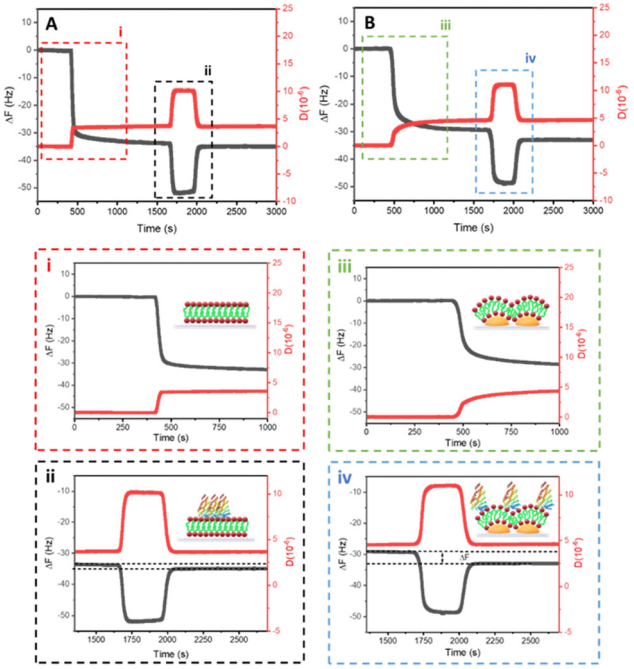

Fig. 4 QCM-D frequency (black) and dissipation (red) profiles of the formation of the DOPC liposome fusion and bilayer formation (i and iii) and CALM interaction (ii and iv) on (A) flat and (B) Pt NP array surfaces.

contributing to the observed dissipation differences. These findings underscore the impact of nanoscale topography on bilayer viscoelastic properties.

As a final step in our work, we address a fundamental question: does lipid topography influence protein spatial distribution? In living cells, lipid membranes undergo dynamic topographical changes, which can have profound effects on protein interactions. To investigate this, we examined how local membrane curvature affects protein binding. CALM, which is able to sense membrane curvature, as well as promote membrane deformation.[36] Preliminary DLS experiments validated the interaction between CALM and the lipid bilayer in solution. When DOPC liposomes were exposed to increasing concentrations of CALM, their diameter increased significantly, from 100 nm to 300 nm, confirming a favourable interaction between CALM and DOPC lipid membranes (Fig. S2B, ESI†).

The interaction between CALM and DOPC bilayers on planar and curved surfaces was monitored by QCM-D. Upon the addition of CALM to previously assembled DOPC SLBs (Fig. 4i and iii), a significant decrease in ΔF was observed (Fig. 4ii and iv). This frequency drop indicates that CALM is interacting with the bilayer. After a washing step with buffer solution, the frequency changes gradually stabilized at $\delta F = \Delta F_{DOPC} - \Delta F_{CALM} \approx$ 2 Hz and 5 Hz for the flat and curved surfaces, respectively. These stabilized values indicate the persistent binding of CALM, with a stronger interaction observed for the curved surface, emphasizing the influence of local membrane curvature on CALM binding affinity. These differences in frequency changes were consistently observed, indicating a stronger binding affinity of CALM influenced by the local curvature of the DOPC membranes formed on the Pt NP array (Fig. S3, ESI†). To confirm this trend, a higher concentration of CALM solution (2 μM compared to 0.5 μM) led to more pronounced changes (Fig. S4, ESI†) Nonetheless, the overall trend remained consistent, with greater CALM interaction observed on the curved bilayer. These results clearly demonstrate that curved bilayers recruit a higher number of CALM proteins, emphasizing the significant influence of membrane curvature on CALM binding.

Dissipation measurements (ΔD) of viscoelastic behaviour provide further insight into both the formation of DOPC bilayers and the interaction with CALM. After DOPC liposomes fusion, ΔD values reached typical ranges for DOPC bilayers (3–6 ppm), confirming successful bilayer formation.[21] The observed increase in ΔD after CALM addition is consistent with protein adsorption onto the lipid bilayer. However, after a washing step, even though CALM is still bound to the membrane, according to the QCM-D analysis, the ΔD values stabilized at levels similar to those of the pristine curved and planar lipid bilayer, respectively. This suggests that CALM forms a layer on top of membranes, irrespective of curvature or flatness, with minimal impact on the membrane's overall viscoelastic properties (Fig. S3C and D, ESI†).[15] Only at starting higher CALM concentrations on flat membranes is a change in dissipation observed after the wash, suggesting the protein has altered the membrane's viscoelastic properties.

AFM measurements corroborated QCM-D results regarding the observed differences in CALM's binding to DOPC bilayers in response to membrane curvature. Representative topographical AFM micrographs of the QCM-D sensor surfaces after CALM binding are shown in Fig. 5. On flat DOPC bilayers, CALM formed large clusters as large as 1 μm across the membrane surface (Fig. 5A). Conversely, CALM distributed more homogeneously on locally curved DOPC membranes, with no observable aggregation (Fig. 5B). The dimensions of the observed objects are consistent with individual CALM proteins, measuring

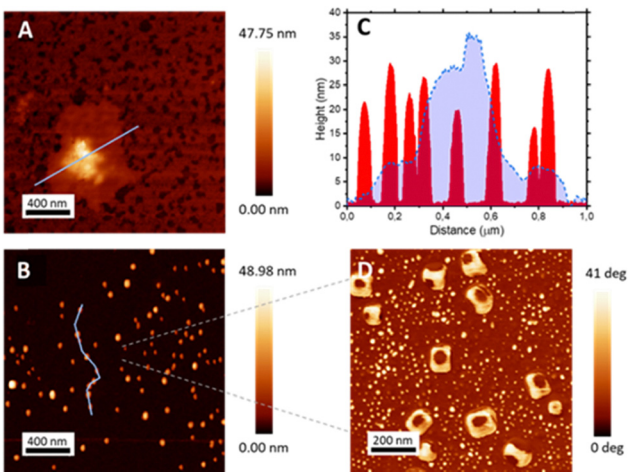

Fig. 5 AFM topographical micrographs of (A) flat membranes after interaction with CALM and (B) curved membranes after CALM binding. (C) Topographical profile comparing flat and curved membranes (obtained from corresponding blue lines in AFM micrographs). (D) AFM phase micrograph of the curved membranes after calm interaction.

approximately 40–50 nm. Topographical profiles (Fig. 5C) further support these observations.

Given that the size of the Pt NPs is on the order of 15–20 nm, it may prevent CALM proteins from interacting with the negatively curved membrane regions between the dots. Therefore, we can assume that CALM preferentially associates with the apex of the Pt array mounds, where the membrane exhibits positive curvature. This nanostructured array has thus highlighted the crucial role of membrane topology in CALM binding. Curvature has been proposed to introduce membrane defects, which would locally appear as having lower lateral membrane pressure. The observation presented here corroborates recent tensiometry measurements, which demonstrated that CALM binds with higher affinity to lipid monolayers under lower lateral pressure, suggesting a preference for binding a curvature.

The stability of the Pt NP array throughout the process is confirmed by the AFM phase image in Fig. 5D. Due to the significant contrast between the hard, metallic particles and the soft DOPC membrane, the Pt nanoparticles remain clearly visible, demonstrating that the nanostructured substrate maintains its integrity during lipid bilayer formation and subsequent protein interactions.

Conclusions

In conclusion, this study successfully demonstrated the use of BCP lithography to fabricate nanostructured surfaces capable of inducing controllable local membrane curvature in lipid bilayers. Lipid bilayer formation was confirmed through AFM and GISAXS analysis over large surface areas. The interaction between CALM protein and DOPC bilayers was then explored, revealing a preferential affinity of CALM for curved membranes. This was evidenced by the more homogeneous protein distribution on curved surfaces compared to flat membranes, as confirmed by both QCM-D and AFM analyses. The distribution of CALM on curved DOPC bilayers suggests that membrane curvature plays a role in modulating CALM's function. The curved membrane intermediates, essential for vesicle budding, likely favour CALM's uniform distribution, preventing the formation of CALM clusters that could hinder the assembly of the endocytic machinery or impede membrane scission. This curvature-driven distribution promotes specific interactions with other endocytic proteins, facilitating CALM's direct involvement in various stages of vesicle formation, from cargo selection to membrane invagination and vesicle pinching. These findings offer new insights into membrane dynamics and protein interactions, with important implications for biological processes like clathrin-mediated endocytosis. The development of nanostructured platforms enables more accurate biomimetic studies, where membrane–protein interactions are critical. Overall, this work highlights the versatility of BCP lithography as a powerful tool for studying the effects of curvature on membrane behaviour and, by extension, its implications for cellular functions. Future research will aim to refine BCP patterning to achieve greater control over membrane curvature by tuning nanoparticle dimensions through adjustments in BCP molecular weight. This platform offers a robust strategy for probing curvature-dependent protein interactions under well-defined conditions, providing clear advantages compared to other nanofabrication methods (see Table S1, ESI†). Moreover, while this study centred on CALM at physiologically relevant concentrations, future work will explore how local protein levels influence curvature sensing and clustering. Incorporating cytoskeletal and ECM components, as well as testing other curvature-sensitive proteins like Epsin and EHD1, will further extend the platform's applicability. Finally, the fabrication methodology presented here is compatible with metallic nanoparticle formation (*e.g.*, gold nanoparticles), opening opportunities for integrating advanced characterization tools such as surface-enhanced Raman scattering (SERS).

Author contributions

L. S. M.: methodology, investigation. D. J. O.: investigation. N. R. Z.: investigation. A. M.: resources, project administration, supervision, funding acquisition. A. A. F.: conceptualization, supervision, investigation, data analysis, writing – original draft, resources. All authors: writing – review & editing.

Data availability

The data supporting this study are available upon request from the corresponding authors.

Conflicts of interest

There are no conflicts to declare.

Acknowledgements

The authors thank the ALBA Synchrotron for the allocation of beam time (ID 2024028341). GISAXS experiments were performed at the BL11 beamline at ALBA Synchrotron in collaboration with ALBA staff. A. M. acknowledges the financial support from MICINN under grant PID2021-129054NA-I00, and from the Department of Education of the Basque Government under grant PIBA-2023-1-0054. A. A. F. is grateful for support from the Provincial Council of Gipuzkoa under the program Fellow Gipuzkoa.

Notes and references

1 K. Jacobson, E. D. Sheets and R. Simson, *Science*, 1979, **1995**(268), 1441–1442.
2 Y.-H. M. Chan and S. G. Boxer, *Curr. Opin. Chem. Biol.*, 2007, **11**, 581–587.
3 L. C. Kam, *J. Struct. Biol.*, 2009, **168**, 3–10.
4 H. Eto, H. G. Franquelim, M. Heymann and P. Schwille, *Soft Matter*, 2021, **17**, 5456–5466.

5 R. J. Brea, M. D. Hardy and N. K. Devaraj, *Chem. – Eur. J.*, 2015, **21**, 12564–12570.
6 P. Schwille, J. Spatz, K. Landfester, E. Bodenschatz, S. Herminghaus, V. Sourjik, T. J. Erb, P. Bastiaens, R. Lipowsky, A. Hyman, P. Dabrock, J. Baret, T. Vidakovic-Koch, P. Bieling, R. Dimova, H. Mutschler, T. Robinson, T.-Y. D. Tang, S. Wegner and K. Sundmacher, *Angew. Chem., Int. Ed.*, 2018, **57**, 13382–13392.
7 S. Höning, D. Ricotta, M. Krauss, K. Späte, B. Spolaore, A. Motley, M. Robinson, C. Robinson, V. Haucke and D. J. Owen, *Mol. Cell*, 2005, **18**, 519–531.
8 X. Wang, H. Du, Z. Wang, W. Mu and X. Han, *Adv. Mater.*, 2021, **33**, 2002635.
9 X. Cheng and J. C. Smith, *Chem. Rev.*, 2019, **119**, 5849–5880.
10 K. Simons and M. J. Gerl, *Nat. Rev. Mol. Cell Biol.*, 2010, **11**, 688–699.
11 Y. Wang, X. Xu, X. Chen and J. Li, *Adv. Mater.*, 2022, **34**, 2107406.
12 K. Corral-Nájera, G. Chauhan, S. O. Serna-Saldívar, S. O. Martínez-Chapa and M. M. Aeinehvand, *Microsyst. Nanoeng.*, 2023, **9**, 107.
13 Y. Zhang, Q. Chen, Y. Zhu, M. Pei, K. Wang, X. Qu, Y. Zhang, J. Gao and H. Qin, *Med. Commun.*, 2022, **3**, e192.
14 L. Sun, Z. Xiong, F. Shen, Z. Wang and Z. Liu, *Sci. China: Chem.*, 2021, **64**, 719–733.
15 I. K. Jarsch, F. Daste and J. L. Gallop, *J. Cell Biol.*, 2016, **214**, 375–387.
16 C. Has, P. Sivadas and S. L. Das, *J. Membr. Biol.*, 2022, **255**, 237–259.
17 H.-Y. Lou, W. Zhao, Y. Zeng and B. Cui, *Acc. Chem. Res.*, 2018, **51**, 1046–1053.
18 K. A. Sochacki, B. L. Heine, G. J. Haber, J. R. Jimah, B. Prasai, M. A. Alfonzo-Méndez, A. D. Roberts, A. Somasundaram, J. E. Hinshaw and J. W. Taraska, *Dev. Cell*, 2021, **56**, 1131–1146.e3.
19 S. E. Miller, S. Mathiasen, N. A. Bright, F. Pierre, B. T. Kelly, N. Kladt, A. Schauss, C. J. Merrifield, D. Stamou, S. Höning and D. J. Owen, *Dev. Cell*, 2015, **33**, 163–175.
20 G. Drin, J.-F. Casella, R. Gautier, T. Boehmer, T. U. Schwartz and B. Antonny, *Nat. Struct. Mol. Biol.*, 2007, **14**, 138–146.
21 R. P. Richter, R. Bérat and A. R. Brisson, *Langmuir*, 2006, **22**, 3497–3505.
22 N. Pawar, M. Peña-Figueroa, E. Verde-Sesto, A. Maestro and A. Alvarez-Fernandez, *Small*, 2024, **20**, 2406885.
23 A. Khakimzhan, Z. Izri, S. Thompson and V. Noireaux, *Biophys. J.*, 2023, **122**, 230a–231a.
24 P.-Y. Yeh, J.-Y. Chen, M.-Y. Shen, T.-F. Che, S. C. Lim, J. Wang, W.-S. Tsai, C. W. Frank, C.-J. Huang and Y.-C. Chang, *J. Mater. Chem. B*, 2023, **11**, 8159–8169.
25 F. Mazur, M. Bally, B. Städler and R. Chandrawati, *Adv. Colloid Interface Sci.*, 2017, **249**, 88–99.
26 J. Kurniawan, J. F. Ventrici de Souza, A. T. Dang, G. Liu and T. L. Kuhl, *Langmuir*, 2018, **34**, 15622–15639.
27 J. Generosi, C. Castellano, D. Pozzi, A. C. Castellano, R. Felici, F. Natali and G. Fragneto, *J. Appl. Phys.*, 2004, **96**, 6839–6844.
28 S. R. Tabaei, J.-H. Choi, G. Haw Zan, V. P. Zhdanov and N.-J. Cho, *Langmuir*, 2014, **30**, 10363–10373.
29 C.-H. Lu, C.-T. Tsai, T. Jones, V. Chim, L. H. Klausen, W. Zhang, X. Li, Z. Jahed and B. Cui, *Biomater. Sci.*, 2023, **11**, 5205–5217.
30 A. Biswas, I. S. Bayer, A. S. Biris, T. Wang, E. Dervishi and F. Faupel, *Adv. Colloid Interface Sci.*, 2012, **170**, 2–27.
31 J. Y. Kim, H. Kim, B. H. Kim, T. Chang, J. Lim, H. M. Jin, J. H. Mun, Y. J. Choi, K. Chung, J. Shin, S. Fan and S. O. Kim, *Nat. Commun.*, 2016, **7**, 12911.
32 A. Alvarez-Fernandez, K. Aissou, G. Pécastaings, G. Hadziioannou, G. Fleury and V. Ponsinet, *Nanoscale Adv.*, 2019, **1**, 849–857.
33 J. Suthar, A. Alvarez-Fernandez, E. Osarfo-Mensah, S. Angioletti-Uberti, G. R. Williams and S. Guldin, *Nanoscale Horiz.*, 2023, **8**, 460–472.
34 N. Paracini, P. Gutfreund, R. Welbourn, J. F. Gonzalez-Martinez, K. Zhu, Y. Miao, N. Yepuri, T. A. Darwish, C. Garvey, S. Waldie, J. Larsson, M. Wolff and M. Cárdenas, *ACS Appl. Mater. Interfaces*, 2023, **15**, 3772–3780.
35 T. H. Anderson, Y. Min, K. L. Weirich, H. Zeng, D. Fygenson and J. N. Israelachvili, *Langmuir*, 2009, **25**, 6997–7005.
36 S. E. Miller, S. Mathiasen, N. A. Bright, F. Pierre, B. T. Kelly, N. Kladt, A. Schauss, C. J. Merrifield, D. Stamou, S. Höning and D. J. Owen, *Dev. Cell*, 2015, **33**, 163–175.